

Absolute three-dimensional micro surface profile measurement based on a Greenough-type stereomicroscope

This content has been downloaded from IOPscience. Please scroll down to see the full text.

2017 Meas. Sci. Technol. 28 045004

(<http://iopscience.iop.org/0957-0233/28/4/045004>)

View [the table of contents for this issue](#), or go to the [journal homepage](#) for more

Download details:

This content was downloaded by: huyanjackson

IP Address: 219.230.110.5

This content was downloaded on 13/02/2017 at 09:10

Please note that [terms and conditions apply](#).

You may also be interested in:

[Defocusing rectified multi-frequency patterns for high-precision 3D measurement](#)

Hai-Qing Huang, Xiang-Zhong Fang and Wei Zhang

[Multiple spatial-frequency fringes selection for absolute phase recovery](#)

Yi Ding, Jiangtao Xi, Yanguang Yu et al.

[3D shape measurement for moving scenes using an interlaced scanning colour camera](#)

Senpeng Cao, Yiping Cao, Mingteng Lu et al.

[Calibration of a camera--projector measurement system and error impact analysis](#)

Junhui Huang, Zhao Wang, Qi Xue et al.

[Camera calibration based on the back projection process](#)

Feifei Gu, Hong Zhao, Yueyang Ma et al.

[Simplified fringe order correction for absolute phase maps recovered with multiple-spatial-frequency fringe projections](#)

Yi Ding, Kai Peng, Lei Lu et al.

[Simplification of high order polynomial calibration model for fringe projection profilometry](#)

Liandong Yu, Wei Zhang, Weishi Li et al.

[Least-squares calibration method based on a universal phase and height mapping formula in Fourier transform profilometry](#)

Yongfu Wen, Haobo Cheng, Ya Gao et al.

[Measuring the 3D shape of high temperature objects using blue sinusoidal structured light](#)

Xianling Zhao, Jiansheng Liu, Huayu Zhang et al.

Absolute three-dimensional micro surface profile measurement based on a Greenough-type stereomicroscope

Yan Hu^{1,2}, Qian Chen², Tianyang Tao^{1,2}, Hui Li^{1,2} and Chao Zuo^{1,2,3}

¹ Smart Computational Imaging (SCI) Laboratory, Nanjing University of Science and Technology, Nanjing, Jiangsu Province 210094, People's Republic of China

² Jiangsu Key Laboratory of Spectral Imaging & Intelligent Sense, Nanjing University of Science and Technology, Nanjing, Jiangsu Province 210094, People's Republic of China

E-mail: huanjackson@163.com and surpasszuo@163.com

Received 6 September 2016, revised 21 December 2016

Accepted for publication 18 January 2017

Published 10 February 2017



Abstract

Fringe projection profilometry has become a widely used method in 3D shape measurement and 3D data acquisition for the features of flexibility, noncontactness, and high accuracy. By combining fringe projection setup with microscopic optics, the fringe pattern can be projected and imaged within a small area, making it possible for measuring 3D surfaces of micro-components. In this paper, a Greenough-type stereomicroscope arrangement is firstly applied for this situation by using the two totally separated and coaxial optical paths of the stereomicroscope. The calibration framework of the stereomicroscope-based system is proposed, which enables high-accuracy calibration of the optical setup for quantitative measurement with the effect of lens distortion eliminated. In the process of 3D reconstruction, depth information is firstly retrieved through the phase-height relation calibrated by a nonlinear fitting algorithm, and the transverse position can be subsequently obtained by solving the equations derived from the calibrated model of the camera. Experiments of both calibration and measurements are conducted and the results reveal that our system is capable of conducting fully automated 3D measurements with a depth accuracy of approximately $4\ \mu\text{m}$ in a volume of approximately $8(L)\ \text{mm} \times 6(W)\ \text{mm} \times 3(H)\ \text{mm}$.

Keywords: phase measurement, three-dimensional sensing, calibration, binocular vision and stereopsis

(Some figures may appear in colour only in the online journal)

1. Introduction

With the development of modern manufacturing technology, miniaturization of devices becomes increasingly important for it can make devices more complex and multi-functional, allowing the manufacture of portable, implantable, or even injectable device. At the same time, characterization of micro-components like MEMS at different manufacturing stage is of great importance. Dynamic measurement is also

³ Author to whom any correspondence should be addressed.

needed in the final devices to test their performance and characteristics, especially 3D imaging of microstructure. Some recently developed techniques, such as confocal microscopy [1], white light interferometry (WLI) [2] and digital holography microscopy (DHM) [3, 4] can be used in surface profilometry of micro-objects. However, confocal microscopy has its disadvantage in measurement speed even though it can offer high resolution, while both WLI and DHM need complex optical paths to generate interferometric fringe. These disadvantages limit their applications in a fast and convenient 3D measurement of small samples. Different from the

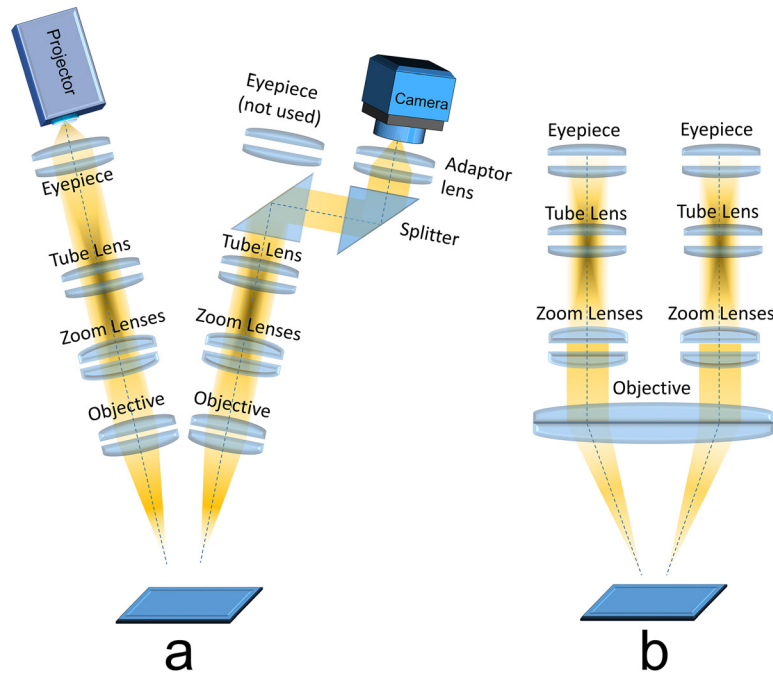


Figure 1. Simplified models of Greenough-type and CMO stereomicroscopes. (a) The path of light rays in the Greenough-type stereomicroscope of our system. (b) The path of light rays in a CMO stereomicroscope.

mentioned methods above, fringe projection profilometry (FPP) has the feature of flexibility, noncontactness and high accuracy, rendering it a widely used technique in 3D shape measurement of macro objects [5–10].

When applying FPP to 3D measurement of micro-scale objects, people need micro-vision instruments to provide magnification for both the projector and the camera so that the fringe pattern can be projected and imaged within a small area. Combining FPP with a stereo micro-vision system, one can retrieve depth information [11–13]. Relevant literature mainly addresses two kinds of systems based on stereo micro-vision instruments: telecentric lenses based and common main objective (CMO) stereomicroscopes based. Recent studies reveal that cameras with telecentric lens can be accurately calibrated using general parameters [14, 15]. Li and Zhang [16] proposed a calibration method for a microscopic structured light system, which successfully utilizes perspective and telecentric models to represent two optical paths, respectively. However, in this system the fringe pattern is projected directly on the object without passing through a magnification optical path, leading to low fringe density and signal to noise ratio [17]. The recently proposed telecentric 3D profilometry using double telecentric lenses [18] improves the performance. However, the fixed parameters of the lenses make it difficult to completely match the field of view (FOV) of the camera and the region of projection. Stereomicroscopes, as another kind of stereo micro-vision instrument, can supply dual views for 3D observation, which provides another valid way to profile the surface of small objects [13, 19–21]. The commonly used CMO stereomicroscope has a specially installed objective shared by both optical paths, which could lead to image distortions typically

exceeding one or two pixels due to the non-paraxial optics [22]. This property makes it difficult to precisely calibrate optical systems based on CMO stereomicroscopes. Another type of commonly used stereomicroscope, named Greenough-type, has two totally separate coaxial optical paths, which are much easier to be calibrated.

In this paper, we propose an accurate calibration-based measurement system to profile the surface of micro-scale objects by using both optical paths of a Greenough-type stereomicroscope. A camera and a projector are fixed on the stereomicroscope, which enables the stereomicroscope to conveniently conduct 3D quantitative measurements. A perspective model considering lens distortion [16, 23, 24] is used to calibrate the camera optical path, which takes advantage of the flexibility and high accuracy of the classic planar camera calibration technique. The projector and the other optical path of the stereomicroscope compose the projection part of the system. This optical part is more complex, making the projector difficult to be calibrated by general parameters. Instead, we set up a relation between depth and phase value in each pixel of the camera by a polynomial fitting method after measuring phase values of a series of planes perpendicular to z direction in different depths [25, 26]. In the 3D reconstruction process, the unwrapped phase value modulated by the object is firstly calculated using the multi-frequency projection technique [27, 28]. Then, the absolute height value in each pixel can be derived through the proposed phase-height relation. After the distortion is compensated in the CCD plane, each pixel of the camera offers three governing equations based on the perspective model. Therefore the corresponding 3D position can be totally derived accordingly.



Figure 2. Physical map of our micro-3D surface profile measurement system based on a Greenough-type stereomicroscope.

2. Measurement principle

2.1. Properties of stereomicroscopes

A Greenough-type stereomicroscope is used as the basic instrument in our measurement system. As shown in figure 1(a), a Greenough-type stereomicroscope is composed of two totally separate coaxial optical paths, while a single large objective shared by both optical paths can be seen in a CMO stereomicroscope as shown in figure 1(b). Figure 1(a) shows the basic light path in our system. The projector is fixed upon the left eyepiece. The camera is fixed on the microscope through a C-type adapter, which shares the light divided by a beam splitter in another tube of the microscope. A CMO stereomicroscope carries inherent small amounts of off-axis aberrations such as astigmatism, coma, and lateral chromatic aberration. This occurs because each optical channel receives light rays from an off-center region of the large objective instead of directly from the center, where aberrations are at a minimum or practically non-existent in lenses. Hence, compensation for optical aberrations of a Greenough-type stereomicroscope is much less than a CMO design, because the lenses are smaller, axially symmetrical, and do not rely heavily on the light rays passing through the objective periphery. Benefiting from the proper combination of lenses and precise installation, the utilized Greenough-type stereomicroscopes in our system can be easily calibrated using our method, which is introduced in section 3.

The used stereomicroscope in our system is equipped with a zoom system to change the overall magnification from $0.8\times$ to $5\times$. The FOV is inversely proportional to the magnification factor, thus this zoom lens system can be applied to change FOV to accommodate different size of measured objects. Depth of field (DOF) is another important concept in stereomicroscope and is also greatly influenced by the

Table 1. Information of the used fringes with different frequency.

Items	Values			
i (Fringe set)	1	2	3	4
N_i (Phase-shifting step)	4	4	4	12
P_i (Pixel number)	608	152	40	12
K_i (Frequency ratio)	1	4	3.8	3.3
Period number	1	4	15.2	50.6

magnification factor. The DOF is inversely proportional to the magnification factor squared, therefore the DOF will be shorter when a larger magnification is needed to measure a smaller object. The typical FOV of the stereomicroscope varies from 5 mm to 15 mm. Some stereomicroscopes are also equipped with an adapter for plugging a camera onto the stereomicroscope to capture a digital image from its shared optical path as the one used in our experimental setup. This flexible adapter makes it very convenient for the camera to adjust its position and the angle.

2.2. PSFPP Principle

Our 3D surface profile measurement system can be seen in figure 2. Fringe patterns composed of vertical sinusoidal stripes with different periods and phase values are projected by the projector in sequence. The camera records the fringe distorted by the object surface, and the computer analyzes the images to obtain the phase modulated by the object. Based on the calculated phase value and an appropriate calibration method, we can reconstruct the absolute 3D surface shape of the measured object.

To acquire the quantitative information of the fringe distortion caused by the object surface, phase-shifting fringe projection profilometry (PSFPP) is applied to acquire the

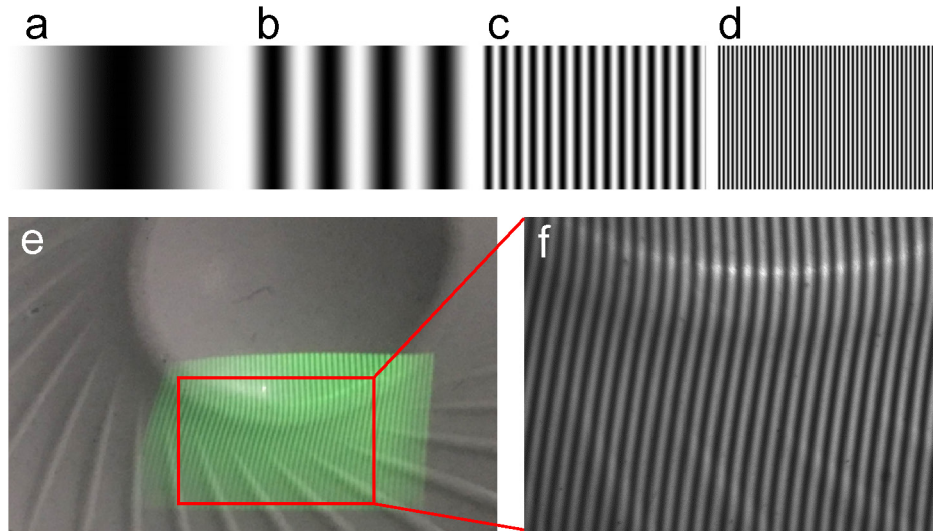


Figure 3. (a)–(d) The four original phase shifting gratings of different period. (e) The measured object of an earphone diagram. (f) The captured image by the camera corresponding to (e).

wrapped phase value of the fringe. The intensity of the fringe image with a phase shift ($2\pi/N$) can be written as

$$I_n(u, v) = A(u, v) + B(u, v) \cos [\Phi(u, v) + 2\pi n/N], \quad (1)$$

where n is the phase-shift index, N is the total number of phase shift and (u, v) is the pixel coordinates. In the rest part of this paper, CCD coordinates (u, v) is omitted for simplicity. A and B are the background intensity and modulation of the fringe, respectively. Φ is the absolute phase value. The wrapped phase ϕ corresponding to Φ can be calculated by least-squares algorithm [29]

$$\phi = -\arctan \frac{\sum_{n=1}^N I_n \sin(2\pi n/N)}{\sum_{n=1}^N I_n \cos(2\pi n/N)}. \quad (2)$$

Due to the periodic nature of the N -step phase-shifting algorithm, we get $\sum_{n=1}^N \cos(\phi + 2\pi n/N) = 0$. Therefore, the average intensity A can be calculated by

$$A = \frac{\sum_{n=1}^N I_n}{N}, \quad (3)$$

and the intensity modulation B can be calculated by

$$B = \frac{2}{N} \sqrt{\left[\sum_{n=1}^N I_n \sin(2\pi n/N) \right]^2 + \left[\sum_{n=1}^N I_n \cos(2\pi n/N) \right]^2}. \quad (4)$$

In general, two kinds of defective cloud points should be excluded from the result: areas where the projected light is dramatically attenuated because of the low reflectivity of the object and areas where the projected light is totally blocked. Intensity modulation B can be utilized as a reference to exclude incorrect phase values in the reconstruction step. If a pixel has an intensity modulation below the predetermined threshold, the corresponding pixel will be set invalid and will not be reconstructed.

For a better accuracy of the calculated phase value, it is preferred to project fringe patterns with more periods. However, the calculated phase value from equation (2) has the range of $(0, 2\pi]$. This introduces the necessity to remove the ambiguity of fringe order to achieve a continuous phase distribution. To solve this problem, multi-frequency phase unwrapping algorithm [28] is applied by using four sets of fringe patterns with different frequency. Thus, unwrapped phase Φ_i can be derived by adding a certain integer T_i multiplied by 2π upon the wrapped phase ϕ_i :

$$\Phi_i = \phi_i + 2\pi T_i, \quad (5)$$

here $T_i = \text{round} [(K_i \Phi_{i-1} - \phi_i)/2\pi]$, Φ_i and ϕ_i are the unwrapped phase and wrapped phase corresponding to the i th set of fringe, respectively. Particularly, $\Phi_1 = \phi_1$. $\text{round}()$ is the function to get the nearest integer. K_i is the frequency ratio of the adjacent sets of fringes. Details of the utilized patterns are listed in table 1. From general experience, K_i should be no more than 8 to 10 in order to assure the unwrapping accuracy. In our system, K_i is controlled less than 4 to make sure that the phase unwrapping is free from ambiguity. Because the period number of the densest fringe is 50.6 so that at least 4 sets of fringe are needed to realize the phase unwrapping. Figures 3(a)–(d) show the used sinusoidal gratings of different periods. Figures 3(e) and (f) are the measured object of an earphone diagram and one corresponding image captured by the camera. It can be clearly seen that the captured fringe has good fringe contrast even when the fringe is very dense (12 pixels in one period on DMD). The ultimate phase accuracy is guaranteed by the fourth set of fringes with 12-step phase shifting algorithm, which is not sensitive to the harmonics until the 11th and also performs well in denoising. Once the phase value of each CCD pixel is known, the 3D model of the object surface can be directly derived through numerical calculation, which is presented in the following sections in details.

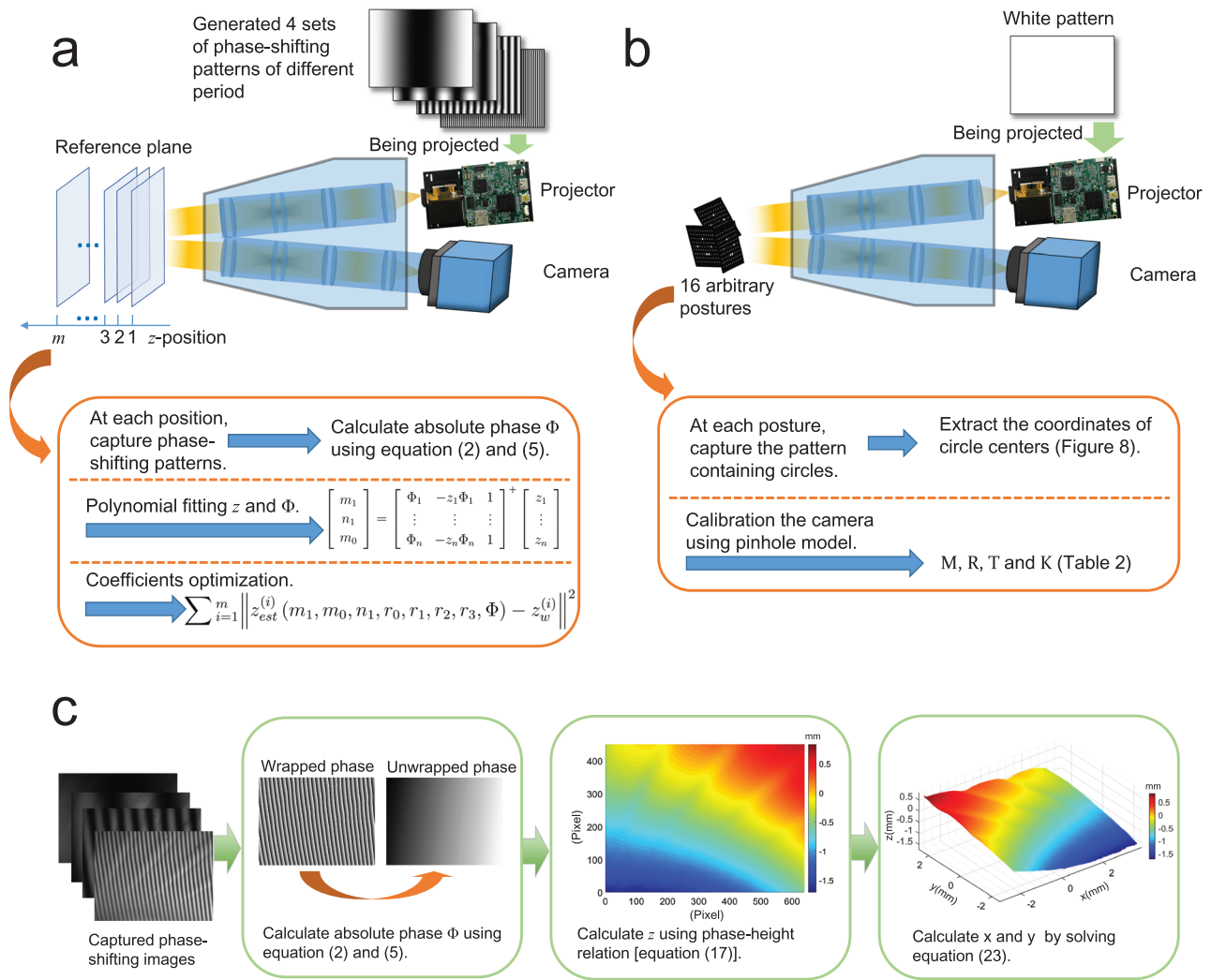


Figure 4. Main process of the system calibration and measurement. (a) Flowchart of the phase-height calibration. (b) Flowchart of the camera calibration. (c) Flowchart of the reconstruction.

3. Calibration principle

The calibration of our system is composed of two parts, which are the phase-height calibration and the camera calibration. The main process of the calibration is given in figure 4. Figures 4(a) and (b) are the flowcharts of the two calibration parts, respectively. Figure 4(c) is the flowchart of 3D reconstruction process. Detailed description of the calibration work is presented in this section.

3.1. Phase-height relation

The stereomicroscope in our system has two totally separate optical paths as shown in figure 1(a). The optical path before the camera contains an objective, zoom lenses, a tube lens and a adapter lens. These lenses are configured coaxially in the tube so that this optical path can be easily calibrated using a perspective model. However, the projector's optical path not only contains the lens belong to the projector itself but also the lenses in the stereomicroscope. The projector's optical axis can hardly coincide with the stereomicroscope, making the traditional calibration method established by several general

parameters inapplicable. Even so, each pixel of the camera corresponds to a geometric relation between the measured phase value and the depth information, which is called the phase-height relation. The determination of this relation is the mainly addressed issue in this section.

The coordinate systems in our system setup are shown in figure 5. $O - XYZ$ denotes the world coordinate system. UV is defined in the CCD plane, and $X_G Y_G$ is defined in the DMD plane. $O_P - X_P Y_P Z_P$ is the projector coordinate system, and $O_C - X_C Y_C Z_C$ is the camera coordinate system. $O_C O_C'$ and $O_P O_P'$ are the optical axis of the camera and the projector, respectively. H and H' mean the principal points of the microscope part, which includes the eyepiece, the tube lenses, the zoom lenses and the objective. The sinusoidal pattern on the DMD varies only in X_G direction, and pixels in the same column have the same phase value. All the light rays originated from pixels on the same column pass through the projection center O_P and make up a plane called equal-phase plane, which is like the plane S_e . In the camera side, each pixel on the camera's CCD also generates a principal line passing through its projection center O_C . For example, pixel P on the CCD plane corresponds to a light ray, which is reflected from point

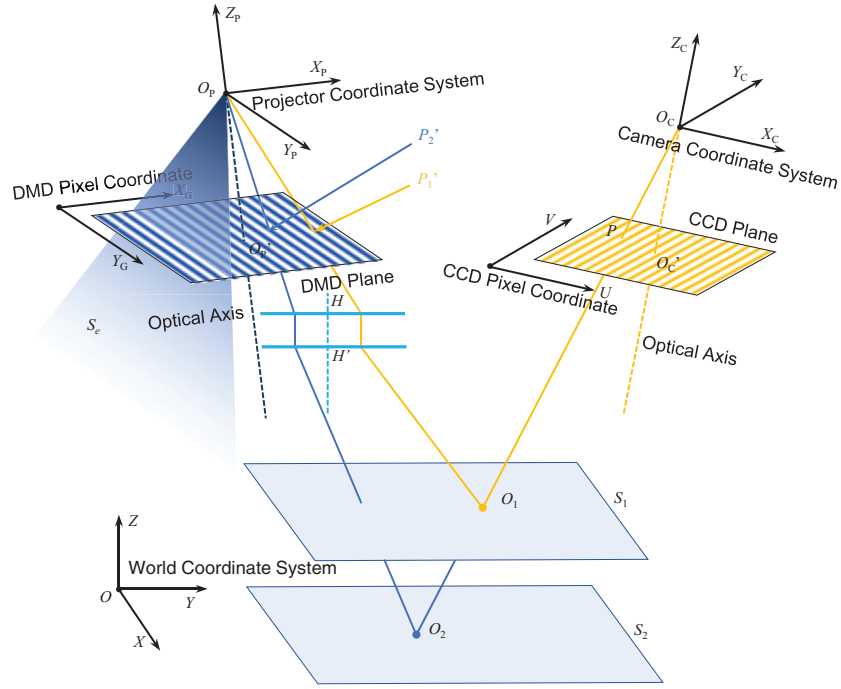


Figure 5. Schematic of the coordinate systems in our setup.

O_1 on surface S_1 and then passes through O_C . Inversely trace this ray into the other optical path, it firstly passes through HH' , then point O_P and intersect the DMD plane at point P_1' at last. The phase value calculated in P on the CCD would be the same as P_1' on the DMD. When the surface S_1 is moved to another position S_2 , The line $O_C P$ will intersect surface S_2 at point O_2 , which denotes a different height on line $O_C P$. The phase value calculated in P will turn into another phase value represented by P_2' on the DMD. This process shows there is a certain relation between the phase value and the depth information in each CCD pixel. Supposing that an arbitrary point $P_P(x_P, y_P, z_P)$ in the projector space corresponds to a point P on CCD, and the projector works in a camera way, which means the fringe pattern loaded on the DMD is the image of the measured object. This imaging process can be expressed as

$$\begin{bmatrix} x_G z_P \\ y_G z_P \\ z_P \end{bmatrix} = \begin{bmatrix} f_{p1} & 0 & p_0 \\ 0 & f_{p2} & p_1 \\ 0 & 0 & 1 \end{bmatrix} \begin{bmatrix} x_P \\ y_P \\ z_P \end{bmatrix}, \quad (6)$$

where, f_{p1} and f_{p2} denote the uniform focal length of the projector lens in X_P and Y_P directions, respectively. p_0 and p_1 are the offset coordinates to the optical axial of the projector. (x_G, y_G) is the image coordinates of P_P . x_G is determined by Φ/k , here Φ is the absolute phase value on the DMD and k is the wave number of the sinusoidal grating. For a certain measured object, as described before, each pixel on the CCD plane corresponds to a line passing through the projector's projection center O_P . All the points on this line satisfy a linear function described in the projector space:

$$x_P = b_1^P z_P + b_0^P, \quad (7)$$

where, b_1^P and b_0^P are constants. Combining equations (6) and (7), we can obtain

$$z_P = \frac{f_{p1} b_0^P}{\Phi/k - p_0 - f_{p1} b_1^P}. \quad (8)$$

Combine another linear function

$$z_P = b_1' z + b_0', \quad (9)$$

where, b_1' and b_0' are constants. We can get the relation between z and Φ as

$$z = \frac{c\Phi + a - bc}{\Phi - b}, \quad (10)$$

where, $a = kf_{p1} b_0^P / b_1'$, $b = k(p_0 + f_{p1} b_1^P)$, and $c = -b_0' / b_1'$. Equation (10) can be simplified as

$$z = \frac{m_1 \Phi + m_0}{n_1 \Phi + 1}, \quad (11)$$

where, $m_1 = -c/b$, $m_0 = c - ab$, and $n_1 = -1/b$. Since all these coefficients are constants, the phase-height relation can be described in a nonlinear expression as equation (11). This nonlinear relation is actually determined by the non-telecentric character of the projector path. The smaller n_1 is, the more linear the relation becomes. It should be noted that each pixel (u, v) of CCD corresponds to its own coefficients written in $m_1(u, v)$, $m_0(u, v)$ and $n_1(u, v)$. We rewrite equation (11) into another form

$$[\Phi \quad -z\Phi \quad 1] [m_1 \quad n_1 \quad m_0]^T = z. \quad (12)$$

This is a linear function with three unknowns: m_1 , m_0 and n_1 . In order to acquire the coefficients, we need at least three pairs of (z, Φ) . The calibration board is placed in a series of predetermined positions along one direction. At each position, sinusoidal patterns in table 1 are continuously projected onto

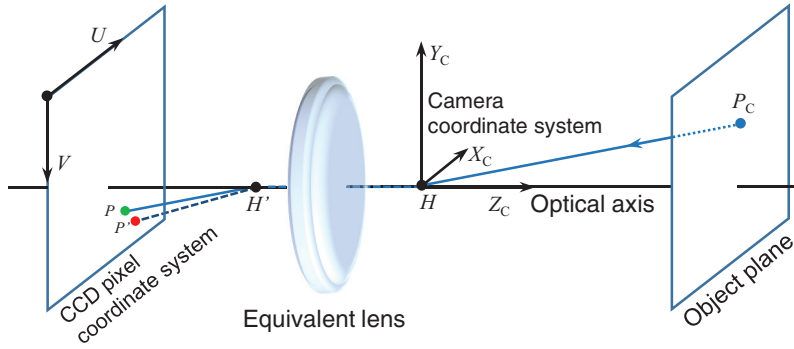


Figure 6. Schematic of the equivalent lens of the camera's optical path.

the board. The unwrapped phase Φ responding to this position is calculated using the algorithm described in section 2. This process needs a repetition when the calibration board is moved into another predetermined depth. After plenty of repetitions, quantity pairs of (z, Φ) are available for curve fitting to evaluate the best coefficients in equation (11). It should be noted that lens distortion in both optical path cannot be omitted. The solution is to add the distortion model into the calibration process. Here we only pay our attention to the radial distortion up to second order. Suppose that in the projector space, a point (x_P, y_P, z_P) corresponds to its real coordinate (x_P', y_P', z_P) with a deviation $[k_{dx}(x_P^2 + y_P^2)x_P, k_{dy}(x_P^2 + y_P^2)y_P]$, which writes

$$\begin{aligned} x_P' &= x_P + k_{dx}(x_P^2 + y_P^2)x_P, \\ y_P' &= y_P + k_{dy}(x_P^2 + y_P^2)y_P. \end{aligned} \quad (13)$$

Here, k_{dx} and k_{dy} are the distortion coefficient. According to equation (7), we have

$$\Delta x_P = b_1^P \Delta z_P. \quad (14)$$

Combining equations (9) and (13), we get the simplified expression as

$$\Delta z = r_3 z^3 + r_2 z^2 + r_1 z + r_0, \quad (15)$$

where, $r_{0,1,2,3}$ are constants that need to be optimized. Thus, the phase-height relation after compensation becomes

$$z = \frac{\Phi m_1 + m_0}{n_1 \Phi + 1} + \sum_{n=0}^3 r_n z^n. \quad (16)$$

Equation (16) can be recognized as the ideal phase-height relation, where the second term represents the distortion that needs to be compensated. On account of the distorted point is very close to its ideal counterpart, we can use z in equation (11) without distortion to replace the expression in equation (16) to retrieve the coefficients

$$z = \frac{\Phi m_1 + m_0}{n_1 \Phi + 1} + \sum_{n=0}^3 \left[r_n \left(\frac{\Phi m_1 + m_0}{n_1 \Phi + 1} \right)^n \right]. \quad (17)$$

In this way, a nonlinear optimization problem with 7 variables is given by

$$\sum_{i=1}^m \|z_{est}^{(i)}(m_1, m_0, n_1, r_0, r_1, r_2, r_3, \Phi) - z_w^{(i)}\|^2. \quad (18)$$

Here, z_{est} is the estimated depth derived from equation (17), z_w is the preset depth and m is the total number of preset depth. The initial value of coefficients m_1, m_0 and n_1 can be determined by the least-mean-squares algorithm for

$$\begin{bmatrix} \Phi_1 & -z_1 \Phi_1 & 1 \\ \vdots & \vdots & \vdots \\ \Phi_m & -z_m \Phi_m & 1 \end{bmatrix} \begin{bmatrix} m_1 \\ n_1 \\ m_0 \end{bmatrix} = \begin{bmatrix} z_1 \\ \vdots \\ z_m \end{bmatrix}, m \geq 3. \quad (19)$$

As much as possible information is desired to make the result more accurate, which means m should be as large as possible. In our work, $m = 30$.

3.2. Camera model and 3D reconstruction

The world coordinate system contains three directions and intuitively three constrains should be offered to make the absolute 3D reconstruction possible. Since the phase-height relation supplies one constraint, the other two constrains should be offered by the calibrated model of the camera. We have known that all the lenses fixed in an optical path of a stereomicroscope are coaxial, therefore these lenses are equivalent to a single lens containing two principal planes as shown in figure 6. Point $P_C(x_C, y_C, z_C)$ in the camera space forms its image point $P(u, v)$ in CCD plane. Based on the pinhole model, we can get [24]

$$\begin{bmatrix} u \\ v \end{bmatrix} = \begin{bmatrix} f_{C1}(x_C/z_C) \\ f_{C2}(y_C/z_C) \end{bmatrix} + \begin{bmatrix} c_0 \\ c_1 \end{bmatrix}, \quad (20)$$

where, f_{C1} and f_{C2} denote the uniform focal length of the camera lens in X_C and Y_C directions, respectively. c_0 and c_1 are the offset coordinates to the optical axial of the camera. However, due to the lens distortion, points in the peripheral area of the FOV may generate its actual image point $P'(u', v')$ deviated from the ideal position $P(u, v)$ on the CCD. The deviation usually contains two parts, radial and tangential distortions. For practical application, compensation for the distortions high to fourth order would be adequate [30]. The distortion in the camera space can be written as

$$\begin{bmatrix} \delta_{x_C} \\ \delta_{y_C} \end{bmatrix} = \begin{bmatrix} (k_1 r_C^2 + k_2 r_C^4)x_C + 2k_3 x_C y_C + k_4(2x_C^2 + r_C^2) \\ (k_1 r_C^2 + k_2 r_C^4)y_C + 2k_4 x_C y_C + k_3(2y_C^2 + r_C^2) \end{bmatrix}. \quad (21)$$

Here, $r_C^2 = x_C^2 + y_C^2$. k_1 and k_2 are the radial distortion coefficients. k_3 and k_4 are the tangential distortion coefficients. The calibration work is accomplished by the Matlab tools. Once the parameters of the camera are calibrated, we can deduce the deviation in the CCD plane and each pixel (u', v') on the CCD would be changed with ideal coordinates (u, v) on the CCD for the following calculation. Combining the ideal coordinates (u, v) with the parameters of the camera, we can get the relation between the pixel coordinates on the CCD and the corresponding 3D position in the world coordinates as

$$w \begin{bmatrix} u \\ v \\ 1 \end{bmatrix} = M[R, T]X = \begin{bmatrix} f_{c1} & \gamma_c & c_0 \\ 0 & f_{c2} & c_1 \\ 0 & 0 & 1 \end{bmatrix} \begin{bmatrix} r_{11} & r_{12} & r_{13} & t_1 \\ r_{21} & r_{22} & r_{23} & t_2 \\ r_{31} & r_{32} & r_{33} & t_3 \end{bmatrix} \begin{bmatrix} x \\ y \\ z \\ 1 \end{bmatrix} = HX. \quad (22)$$

Here, w is the scale factor, $R = [r_{ij}]$, ($i, j = 1, 2, 3$), is the rotation matrix, $T = [t_1, t_2, t_3]^T$ is the translation vector, and $X = [x, y, z, 1]^T$ is the world coordinates. H is the homography matrix, and M contains the intrinsic parameters of the camera. Equation 22 can be expressed in another way

$$\begin{bmatrix} 1 & -h_{11}/u & -h_{12}/u \\ 1 & -h_{21}/v & -h_{22}/v \\ 1 & -h_{31} & -h_{32} \end{bmatrix} \begin{bmatrix} x \\ y \\ w \end{bmatrix} = \begin{bmatrix} (h_{14} + zh_{13})/u \\ (h_{24} + zh_{23})/v \\ h_{34} + zh_{33} \end{bmatrix}. \quad (23)$$

Once H is calibrated, the transverse position $x(u, v)$ and $y(u, v)$ can easily be figured out through equation (23).

It should be made clear that the calibration of the system consists of two parts. As a result, there will be two different world coordinate systems. The unique world coordinate system should be determined by the camera on condition that the $z = 0$ plane of the phase-height relation coincides with the $z = 0$ plane of the camera optical path. A ceramic substrate is used as the calibration board, which has the size of $8 \times 8 \text{ mm}^2$. The top side of the board prints a pattern commonly used in binocular vision calibration as shown in figure 7. The pattern has 99 (9×11) white circular spots. The centre-to-centre spacing between every two adjacent white circles is 0.65 mm. The diameters of big and small circles are 0.4 mm and 0.175 mm, respectively. This pattern is used for camera calibration.

4. Calibration results

Our system is mainly composed of a Greenough-type stereomicroscope, a projector and a camera. The projector is a DLP Light Crafter from *Texas Instruments* with a 608×684 diamond pixel 0.3 inch WVGA DMD. The camera is a DMK 23U445 from *The Imaging Source*, which has the resolution of 1280×960 with *Sony ICX445ALA* CCD of $3.75 \mu\text{m}$ cell size.

4.1. Calibration result of the camera

The camera is calibrated first. As shown in figure 4(b), images containing spot patterns are obtained when the board is placed at 16 different postures. To make the $z = 0$ plane of both calibration parts coincide, when the last image is captured, we should turn this board upside to utilize the white side with no pattern to calibrate the phase-height relation.

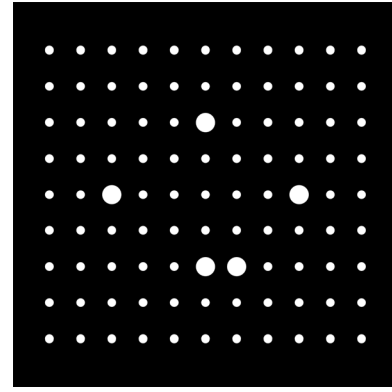


Figure 7. Pattern of the calibration board used in our system. The centre-to-centre spacing between every two adjacent white circles is 0.65 mm. The diameters of big and small circles are 0.4 mm and 0.175 mm, respectively.

This shared posture supplies the $z = 0$ plane of both calibration parts, therefore the unique world coordinate system can be determined.

For the sake of avoiding a singular matrix problem in solving H in equation (22), all the postures should have a rotation angle around one or more axes instead of merely translating it along one direction without changing the normal vector of the plane. However, the FOV and DOF of our system are smaller compared with normal cameras. It is quite possible to come across the singular problem if the data are not enough. To get a more accurate calibration result, more postures should be applied. Figure 8 shows the 16 calibration images containing extracted circle centers.

The estimated parameters are shown in table 2. We can calculate the skew angle of the CCD by $\theta = \arctan(f_{c1}/\gamma_c)$, which is about 90.0025° . This angle is pretty close to 90° as expected with all modern CCD cameras. The distortion coefficients are also very small. A re-projection process was conducted to verify the calibration accuracy. We compared the predicted pixel positions of the pattern's mark points with the corresponding extracted ones. Figure 9 shows the re-projection error distribution. There are total 560 marked points in 16 images, and the root-mean-square error (RMSE) of the re-projection errors in two directions are (0.07206, 0.08591).

4.2. Calibration result of phase-height relation

The phase-height relation in each pixel is calibrated by translating the calibration board along the z direction with a precise translation stage that possesses a precision of $10 \mu\text{m}$. As shown in figure 4(a), the sinusoidal fringe patterns are continuously projected on the plane surface, and the camera captures the images. The phase value can be calculated by equations (2) and (5). Enough phase values are obtained by translating the board along z direction at equally spaced positions with per moved step of $100 \mu\text{m}$. The phase-height relation in 4 random pixels is given as an example in figure 10, which shows a nearly linear relation between phase and height.

To verify the accuracy of the calibrated phase-height relation, we measured a plane perpendicular to z direction. Figure 11(a)

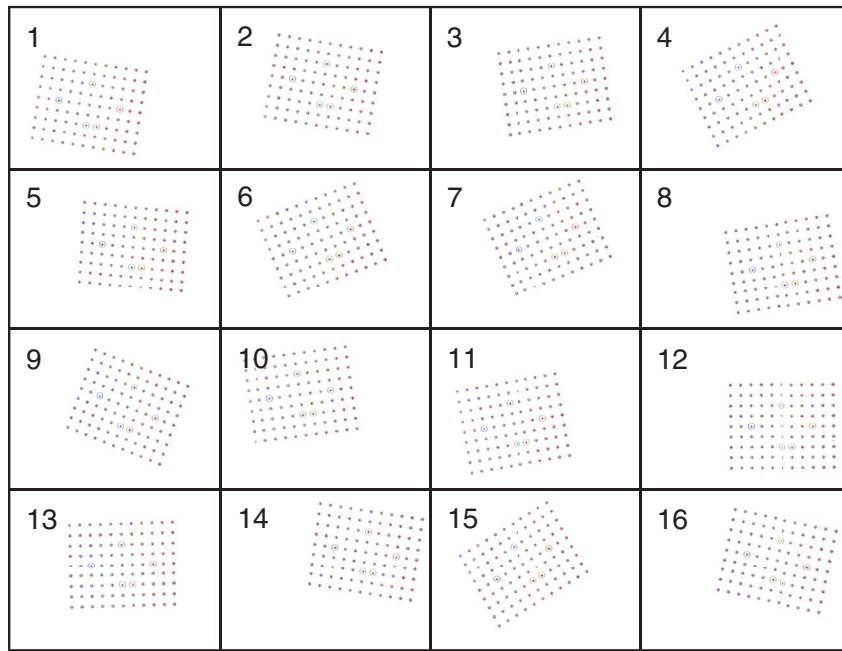


Figure 8. 16 calibration pictures with the circles marked.

Table 2. Calibration result of the camera.

Item	Value
Camera intrinsic matrix \mathbf{M}	$\begin{bmatrix} 22\,683.6612 & -0.9944 & 633.3725 \\ 0 & 22\,760.4770 & 520.4101 \\ 0 & 0 & 1 \end{bmatrix}$
Rotation matrix \mathbf{R}	$\begin{bmatrix} 0.9926 & 0.0724 & -0.0978 \\ 0.0941 & -0.9664 & 0.2391 \\ -0.0772 & -0.2465 & -0.9661 \end{bmatrix}$
Translation \mathbf{T}	$[-3.5782 \quad 6.0773 \quad 224.5595]^T$
Distortion \mathbf{K}	$[-0.095\,31 \quad 0.025\,12 \quad -0.008\,69 \quad -0.002\,73]^T$

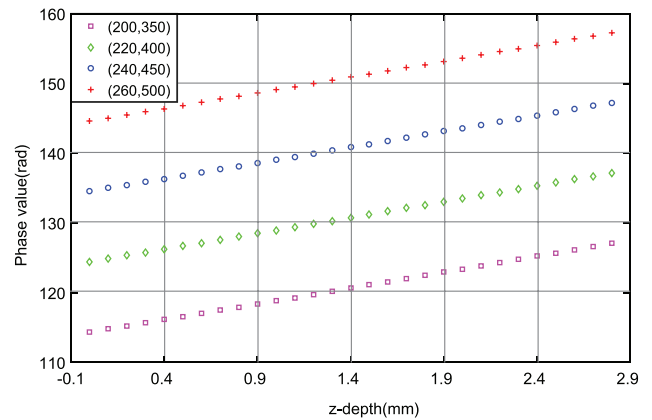


Figure 10. Phase-height relation measured in 4 random pixels.

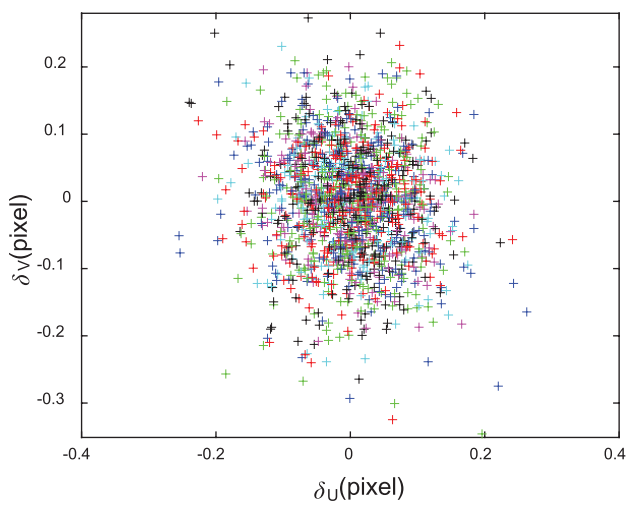


Figure 9. Re-projection errors (in pixel) of the camera model with distortion considered. The RMSE of the re-projection errors in two directions are (0.07206, 0.08591).

shows the color-coded phase value and figure 11(b) shows the derived color-coded depth distribution. Figure 11(c) shows the depth of the 330th line, which indicates a random noise under $4.0 \mu\text{m}$. The root-mean-square error (RMSE) of the measured area is $1.223 \mu\text{m}$. Figure 11(d) gives the histogram of the error statistics, from which we can see that the most errors fall into the range of $\pm 5 \mu\text{m}$.

To further verify the accuracy of the absolute 3D reconstruction, we measured the locations of the circles' centers on the calibration board. The pattern on the board has white circle spots with their centers equally distributed like a 2D comb function. The board is placed under the stereomicroscope in a random posture like figure 12(a). The centers' pixel coordinates can be extracted and the phase values of these centers can also be obtained by PSFPP. Figure 12(b) shows absolute 3D distribution of 35 reconstructed center points marked in the orange rectangle of figure 12(a). The reconstructed positions

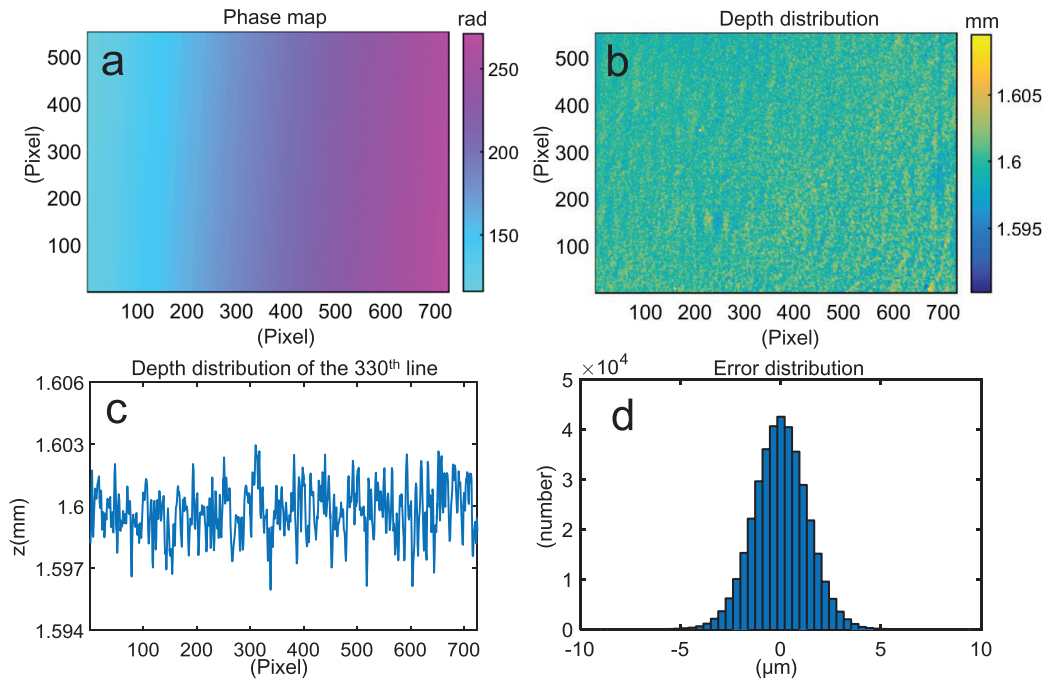


Figure 11. Height measurement result of a plane. (a) Absolute phase map. (b) Depth distribution. (c) Depth distribution of the 330th line of (b). (d) Histogram of the error statistics of (b).

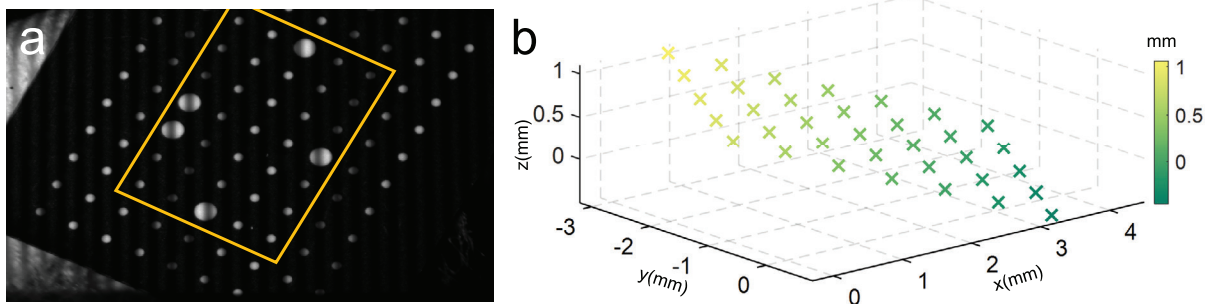


Figure 12. Absolute 3D reconstruction of circles' centers on the calibration board. (a) One of the captured image of the measured board. (b) 3D point cloud distribution of the circles' centers marked in the orange lines in (a).

of these centers are presented by crosses with their depths being color-coded. The distance between two points can be calculated by $d = \|(x_1, y_1, z_1) - (x_2, y_2, z_2)\|^2$, where, d is the distance between two points: (x_1, y_1, z_1) and (x_2, y_2, z_2) . There are total 28 pairs of neighboring centers in the short direction, and 30 pairs of neighboring centers in the long direction. The calculated distances between these neighboring centers have the mathematical expectation of 0.6502 mm and the RMSE of 0.0011 mm, which is pretty close to the standard data (0.65 mm, 0.0015 mm) given by the producer.

5. Measurement results

5.1. Measurement of a partial surface of a coin

Experiments were conducted to measure objects with different kind of shapes. Firstly, we measured a partial surface of a coin as marked in a red circle in figure 13(a).

Figure 13(c) shows one deformed fringe pattern. After phase-height conversion by equation (17), the height distribution corresponding to figure 13(c) can be calculated out as shown in figure 13(b). The absolute 3D reconstruction is obtained through solving equation (23) and the result is given in figure 13(d) with the height information coded by color. The inclined posture relative to the reference plane leads to a depth range about 0.3 mm, which is totally within the measurement range of our setup. This result demonstrates that small objects with embossed surface can be successfully reconstructed.

5.2. Measurement of a TFBGA

In the second experiment, a thin fine-pitch ball grid array (TFBGA) as shown in figure 14(a) with a standard lead pitch of 0.8mm was measured. The absolute 3D distribution of the surface marked with yellow dash line in

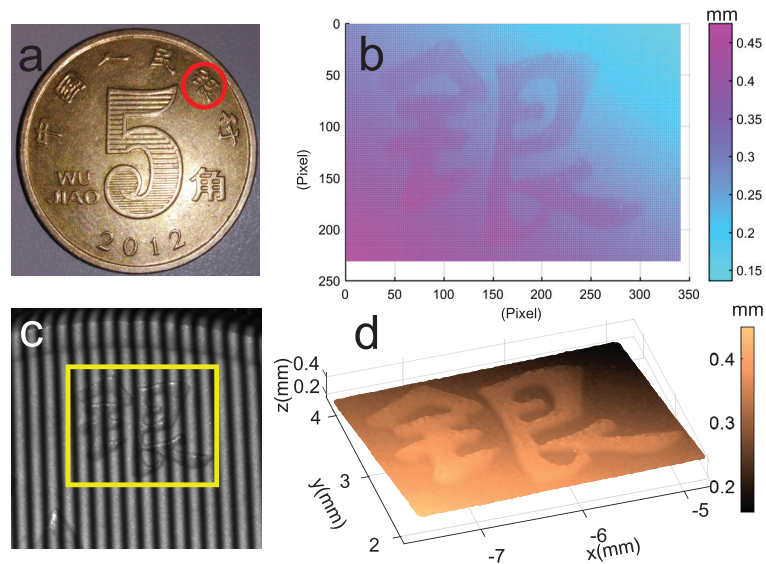


Figure 13. Experimental result of a coin. (a) The measured coin. (b) Height distribution corresponding to the yellow rectangle in (c). (c) One deformed fringe pattern. (d) Absolute 3D reconstruction of the character.

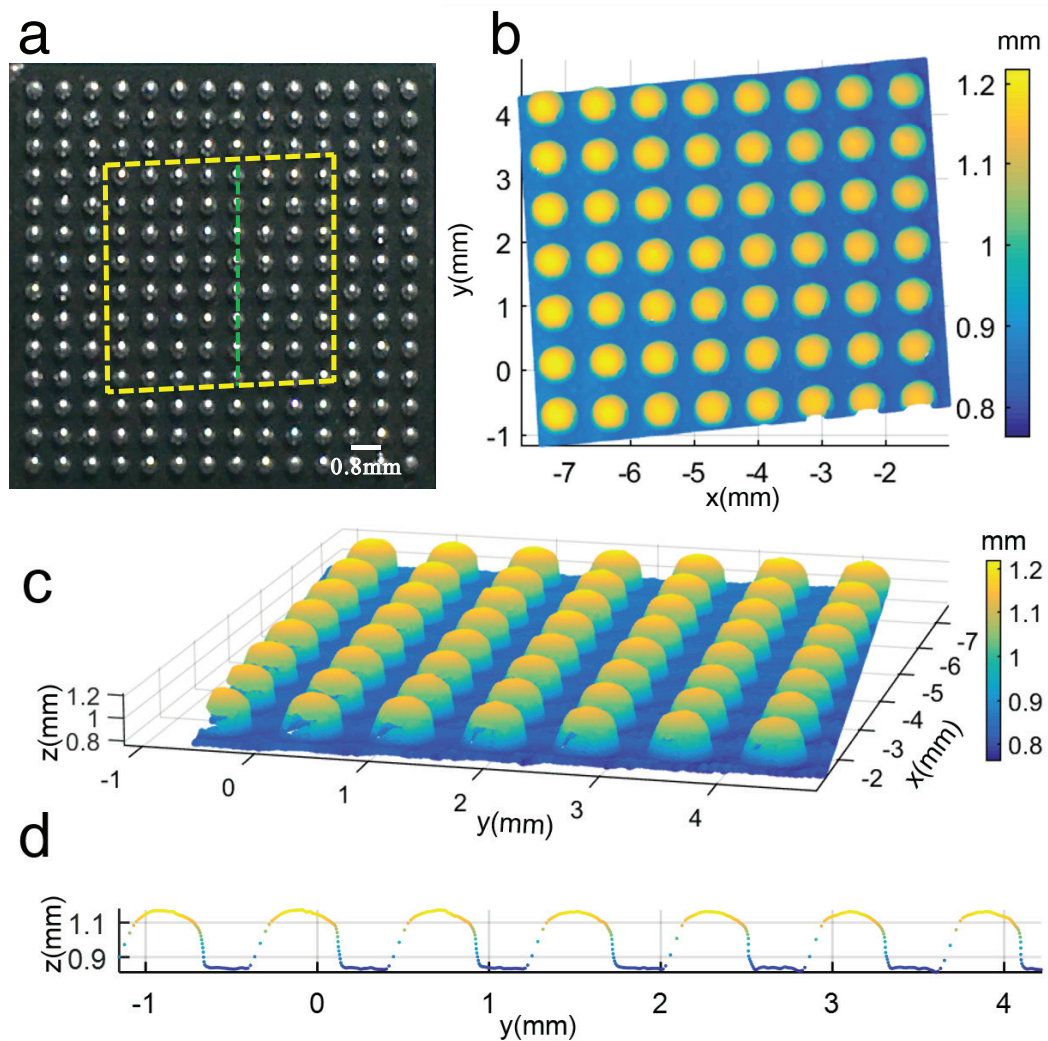


Figure 14. Experimental result of a TFPGA. (a) Picture of the measured TFPGA. (b) Reconstructed 3D data corresponding to the yellow quadrangle in (a). (c) Another view of the 3D data from a different angle. (d) A cross section corresponding to the green line in (a).

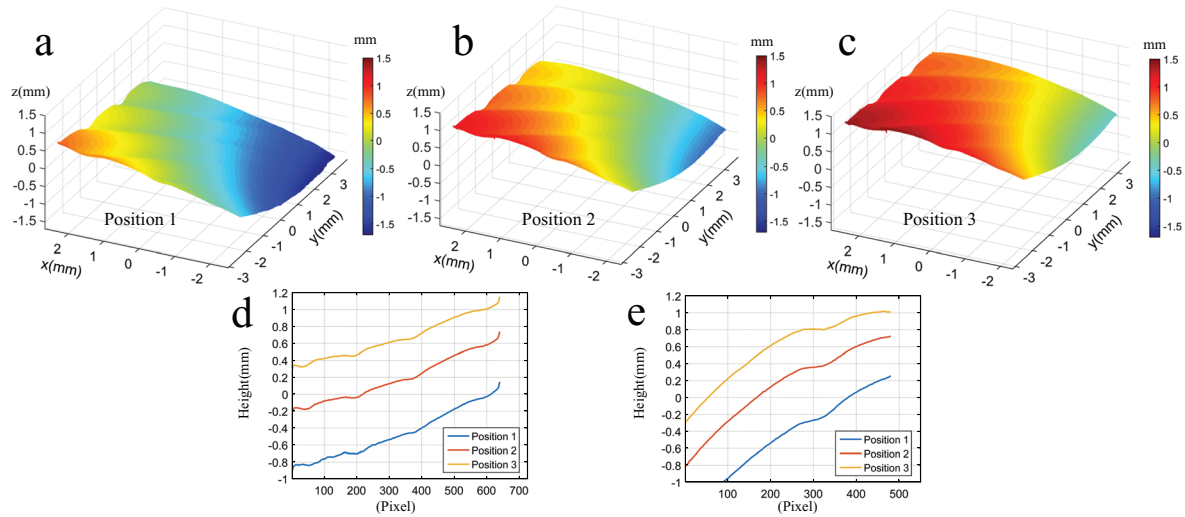


Figure 15. Experimental result of an earphone diaphragm. (a)–(c) 3D reconstruction of the diaphragm at its concave, equilibrated and raised state, respectively. (d) Height information of the 200th row corresponding to three positions. (e) Height information of the 300th column corresponding to three positions.

figure 14(a) is obtained through the same steps described in the first experiment and the result is shown in figure 14(b). Another view of the reconstructed surface from a different angle is presented in figure 14(c), and a cross section corresponding to the green dash line in figure 14(a) is shown in figure 14(d). The most important geometrical features about ball grid array (BGA) are the coplanarity (height variance), spherical degree and radius of the balls. The standard heights and radius of the balls on the measured chip are 0.4 ± 0.05 mm and 0.5 ± 0.05 mm, respectively. From figure 14(c), we can clearly recognize the spherical structures representing the balls. The radius and heights of balls derived from figures 14(c) and (d) considerably accord with the standard data. The obtained 3D data supplies inspectors sufficient information to analyze the features and to detect the defect on the balls.

5.3. Measurement of an earphone diaphragm

In the third experiment, we measured an earphone diaphragm as shown in figure 3(e). The diaphragm was controlled at three different shapes: concave, equilibrated and raised by changing the voltage loaded on the lead wire of the earphone. The measurement result is shown in figure 15. When the diaphragm's state changes, the position of the diaphragm will shift mainly in the vertical direction. Figures 15(a)–(c) are the 3D reconstructions of the diaphragm in concave, equilibrated and raised shapes, respectively. Figure 15(d) gives the height information of the 200th row corresponding to three positions of the diaphragm and figure 15(e) gives the height information of the 300th column corresponding to three positions of the diaphragm. It can be clearly seen that details like the grooves are well reconstructed as shown figures 15(a)–(c). The result also reveals there are at least 3 mm measurement range in z direction of our system.

6. Conclusions

In this paper, a 3D micro-surface profile measurement system based on a Greenough-type stereomicroscope is presented. By combining fringe projection setup with microscopic optics, the imaging model and a dedicated calibration approach are established to realize quantitative 3D imaging of micro-profiles. The effectiveness of proposed system and methods have been completely demonstrated by experiments on system calibration, accuracy evaluation and 3D imaging of micro-shapes like spheres, ramps, planes and grooves. In sum, our system is capable of conducting fully automated 3D measurements with a depth accuracy of approximately $4 \mu\text{m}$ in a volume of approximately $8(\text{L}) \text{ mm} \times 6(\text{W}) \text{ mm} \times 3(\text{H}) \text{ mm}$.

Acknowledgments

This work was supported by '333 Engineering' research project (BRA2015294, Jiangsu Province, China), Fundamental Research Funds for the Central Universities (30915011318), the Research and Innovation Plan for Graduate Students of Jiangsu Higher Education Institutions, China (Grant No. KYLX15_0367), and Open Research Fund of Jiangsu Key Laboratory of Spectral Imaging & Intelligent Sense (3092014012200417).

References

- [1] Tiziani H J, Wegner M and Steudle D 2000 Confocal principle for macro-and microscopic surface and defect analysis *Opt. Eng., Bellingham* **39** 32–9
- [2] Deck L and De Groot P 1994 High-speed noncontact profiler based on scanning white-light interferometry *Appl. Opt.* **33** 7334–8

- [3] Yamaguchi I and Zhang T 1997 Phase-shifting digital holography *Opt. Lett.* **22** 1268–70
- [4] Kim M K 2010 Principles and techniques of digital holographic microscopy *SPIE Rev.* **1** 018005
- [5] Huang L, Ng C S and Asundi A K 2011 Dynamic three-dimensional sensing for specular surface with monoscopic fringe reflectometry *Opt. Express* **19** 12809–14
- [6] Zhang Q and Su X 2005 High-speed optical measurement for the drumhead vibration *Opt. Express* **13** 3110–6
- [7] Zuo C, Chen Q, Gu G, Feng S, Feng F, Li R and Shen G 2013 High-speed three-dimensional shape measurement for dynamic scenes using bi-frequency tripolar pulse-width-modulation fringe projection *Opt. Lasers Eng.* **51** 953–60
- [8] Zhang S 2010 Recent progresses on real-time 3d shape measurement using digital fringe projection techniques *Opt. Lasers Eng.* **48** 149–58
- [9] Tao T, Chen Q, Da J, Feng S, Hu Y and Zuo C 2016 Real-time 3-d shape measurement with composite phase-shifting fringes and multi-view system *Opt. Express* **24** 20253–69
- [10] Feng S, Chen Q, Zuo C and Asundi A 2017 Fast three-dimensional measurements for dynamic scenes with shiny surfaces *Opt. Commun.* **382** 18–27
- [11] Yin Y, Wang M, Gao B Z, Liu X and Peng X 2015 Fringe projection 3d microscopy with the general imaging model *Opt. Express* **23** 6846–57
- [12] Li A, Peng X, Yin Y, Liu X, Zhao Q, Krner K and Osten W 2013 Fringe projection based quantitative 3d microscopy *Optik-Int. J. Light Electron. Opt.* **124** 5052–6
- [13] Zhang C, Huang P S and Chiang F-P 2002 Microscopic phase-shifting profilometry based on digital micromirror device technology *Appl. Opt.* **41** 5896–904
- [14] Li D and Tian J 2013 An accurate calibration method for a camera with telecentric lenses *Opt. Lasers Eng.* **51** 538–41
- [15] Chen Z, Liao H and Zhang X 2014 Telecentric stereo micro-vision system: calibration method and experiments *Opt. Lasers Eng.* **57** 82–92
- [16] Li B and Zhang S 2015 Flexible calibration method for microscopic structured light system using telecentric lens *Opt. Express* **23** 25795–803
- [17] Li J, Hassebrook L G and Guan C 2003 Optimized two-frequency phase-measuring-profilometry light-sensor temporal-noise sensitivity *JOSA A* **20** 106–15
- [18] Li D, Liu C and Tian J 2014 Telecentric 3d profilometry based on phase-shifting fringe projection *Opt. Express* **22** 31826–35
- [19] Windecker R, Fleischer M, Krner K and Tiziani H J 2001 Testing micro devices with fringe projection and white-light interferometry *Opt. Lasers Eng.* **36** 141–54
- [20] Windecker R, Fleischer M and Tiziani H J 1997 Three-dimensional topometry with stereo microscopes *Opt. Eng., Bellingham* **36** 3372–7
- [21] Proll K-P, Nivet J-M, Voland C and Tiziani H J 2000 Application of a liquid-crystal spatial light modulator for brightness adaptation in microscopic topometry *Appl. Opt.* **39** 6430–5
- [22] Danuser G and Kübler O 1991 Calibration of cmc-stereo-microscopes in a micro robot system *Int. Archives of Photogrammetry and Remote Sensing, 30/5W1 (Citeseer)* pp 345–53
- [23] Feng S, Chen Q, Zuo C, Sun J and Yu S L 2014 High-speed real-time 3-d coordinates measurement based on fringe projection profilometry considering camera lens distortion *Opt. Commun.* **329** 44–56
- [24] Zhang Z 2000 A flexible new technique for camera calibration *IEEE Trans. Pattern Anal. Mach. Intell.* **22** 1330–4
- [25] Zhang Z, Ma H, Guo T, Zhang S and Chen J 2011 Simple, flexible calibration of phase calculation-based three-dimensional imaging system *Opt. Lett.* **36** 1257–9
- [26] Liu H, Su W-H, Reichard K and Yin S 2003 Calibration-based phase-shifting projected fringe profilometry for accurate absolute 3d surface profile measurement *Opt. Commun.* **216** 65–80
- [27] Kim E-H, Hahn J, Kim H and Lee B 2009 Profilometry without phase unwrapping using multi-frequency and four-step phase-shift sinusoidal fringe projection *Opt. Express* **17** 7818–30
- [28] Zuo C, Huang L, Zhang M, Chen Q and Asundi A 2016 Temporal phase unwrapping algorithms for fringe projection profilometry: a comparative review *Opt. Lasers Eng.* **85** 84–103
- [29] Malacara D 2007 *Optical Shop Testing* 3rd edn (New York: Wiley)
- [30] Bouguet J Y 2010 Camera calibration toolbox for Matlab www.vision.caltech.edu/bouguetj/calib_doc/